A numerical analysis of heat and fluid flow with a deformable curved free surface in a laser melting process

Young-Deuk Kim [a], Woo-Seung Kim [b,*]

[a] Department of Mechanical Engineering, Hanyang University, 17 Haengdang-dong, Seongdong-gu, Seoul 133-791, Republic of Korea
[b] Department of Mechanical Engineering, Hanyang University, 1271 Sa 3-dong, Sangnok-gu, Ansan, Gyeonggi-do 426-791, Republic of Korea

ARTICLE INFO

ABSTRACT

In this study, a numerical investigation was performed to examine the effects of curved surface shapes, laser power intensity, and the thermophysical properties of a material such as Reynolds and Capillary numbers on the shape, size, and surface topography of the melt pool. This investigation was completed via two-dimensional axisymmetric thermocapillary convection analyses during laser melting processes with deformable free surfaces. In general, a bump has a deep crater at the center and a low peripheral rim, a bowl-like shape. This is caused by the surface temperature gradient-induced thermocapillary flow driving the molten material towards the cooler region, which has higher surface tension. For flat and parabolic free surfaces, surface deformations such as crater depth and rim height increase gradually with decreasing Re and increasing Ca, B_f, and especially the curvature of the free surface. In particular, it is noted that the curvature of the free surface has significantly little effect on the crater depth and rim height for a higher Re and lower B_f with fixed Ca. Its effect is considerably strengthened at a lower Re and higher B_f, indicating stronger convection. In the case of a sinusoidal wavy surface, it is noted that the crater depth and rim height increase monotonically with increasing Ca at fixed Re and B_f, while they decrease with increasing Re and B_f at fixed Ca due to the inward transfer of relatively large amounts of molten material compared to the surface tension gradient driving force, which causes the recovery of the crater center. Hence, the slope of the crater decreases significantly.

© 2008 Elsevier Inc. All rights reserved.

1. Introduction

Laser-assisted melting and surface modification are widely used in industrial processes including welding, cutting, drilling, as well as for the surface treatment of materials because of its high welding strength and speed and a smaller heat-affected region than GTAW (gas tungsten arc welding), CO_2 welding, and other welding processes. In particular, laser sources can provide controllable high-density energy deposition in a specific surface area for producing thin hardened surface layers in a workpiece of metallic material. During laser melting processes, the fluid flow and heat transfer in the molten pool significantly affect the shape, size, and surface topography ("bumps") in the melt pool. The fluid flow in the melt pool is driven primarily by the spatial variation in the surface tension of the molten pool surface, which is caused by the large temperature gradient.

Therefore, numerous investigations dealing with the shape and size of the molten pool as a function of various laser parameters with an undeformable flat surface were performed by two- and three-dimensional numerical simulations (Basu and Date, 1990; Chan et al., 1988; Kim and Sim, 1997; Ravindran et al., 1994; Srinivasan and Basu, 1986). Prior studies showed that buoyancy forces in the molten pool can be neglected (Srinivasan and Basu, 1986), and the scanning velocity plays an insignificant role because of the higher magnitude of the surface tension-driven velocity (Chan et al., 1988; Srinivasan and Basu, 1986).

The transient surface deformations of Ni–P disk substrates and metallic thin films upon pulsed laser heating have been investigated experimentally (Baumgart et al., 1995; Chen et al., 2000; Willis and Xu, 2000). They found several kinds of the surface shapes (V-type bump, sombrero bump, and double-rim bump) resulting from different pulse energies of the heating laser beam. In particular, Chen et al. (2000) showed that surface deformation can be explained as a result of surface tension-induced flow, which depends not only on the surface temperature, but also on the surfactant concentration. They also mentioned that laser heating can at least partially remove the native oxide layer if the induced surface temperature is high enough, and this situation produces a gradient of surfactant concentration which carries the molten material towards the center. Accordingly, if the surfactant compositional effect is dominant during the laser melting process, a sombrero bump is formed on the Ni–P disk substrate.

---

* Corresponding author. Tel.: +82 31 400 5248; fax: +82 31 418 0153.
 E-mail address: wskim@hanyang.ac.kr (W.-S. Kim).

In addition, Fan et al. (2001), Ha and Kim (2005), Ha et al. (2006), Han and Liou (2004), Iwamoto et al. (1998), and Sim and Kim (2005) investigated transient molten pool geometry during a laser melting process with a deformable flat surface. However, Fan et al. (2001) analyzed the fluid flow driven by electromagnetic, buoyancy, arc drag, and thermocapillary forces during stationary GTAW, and considered only surface pressure distribution in tracing the free surface evolution. Ha and Kim (2005) and Ha et al. (2006) used the Eulerian finite difference model to couple a two-dimensional axisymmetric Navier–Stokes equation solver for fluid flow with free surfaces using RIPPLE and an energy equation with a source-based solidification algorithm, along with the volume-of-fluid (VOF) method and the modified continuum surface force (CSF) method to incorporate Marangoni effect with a deformable free surface. They also showed that the bump is shaped like a bowl. Han and Liou (2004) examined the effect of the laser beam mode on the formation and development of the molten pool during the laser material interaction process by three-dimensional numerical analysis. They used the projection method to determine the velocity and pressure and the level set method to track the evolution of the free surface. In this way, they showed that the free surface is a bowl-like shape with a general Gaussian beam mode. Iwamoto et al. (1998) used a simplified equation for predicting the free surface shape of the melt pool and highly simplified marker and cell (HS-MAC) method, and showed that the bump has a bowl shape. Sim and Kim (2005) solved the two-dimensional axisymmetric Navier–Stokes equation with boundary conditions by using a finite volume method employing a SIMPLER algorithm and an energy equation with a source-based method. They determined the free surface shape of the molten pool with a normal stress balance at the gas–fluid interface, liquid volume, and initial and boundary equations. Here, a shooting method was used to find a free integra- tion constant included in the normal stress balance equation. They showed that the shape of the free surface is a bowl bump at a low Re, while at a high Re two kinds of surface shapes occur with time: bowl and sombrero bumps.

As shown in the aforementioned literature, a limited number of numerical simulations for thermocapillary convection in laser sur-face melting with a deformable flat surface have been reported. Furthermore, no numerical analyses on dynamic surface deforma-tion in laser-assisted melting with a curved surface have been dis-cussed in previous research. It is evident that the curvature of the free surface can change the shape, size, and surface topography of the molten pool during laser melting processes, as shown by the flow characteristics of thermocapillary convection on a flat or curved surface (Sim and Zebib, 2002). Furthermore, the laser melt-ing processes for a workpiece with a curved surface could be per-formed more frequently in industrial processes than those for a flat surface. In the present study, we report on the effect of the curva-ture of the free surface on the shape, size, and surface topography of the molten pool via two-dimensional numerical analyses for steady and transient melting and surface deformation in a laser surface melting process with a curved free surface.

2. Mathematical model description

A schematic diagram of a heated laser surface is shown in Fig. 1. To analyze steady and transient melting as well as surface topo-graphic features of the melt pool, laser melting processes with deformable flat, parabolic, and sinusoidal wavy surfaces (which have a ratio of non-dimensional wavelength ($\lambda = 0.55$) to non-dimensional amplitude ($A = 0.05$), $\lambda/A = 11$) are considered in this study. A stationary, continuous, axisymmetric laser beam with a uniform or Gaussian heat flux distribution irradiates the surface
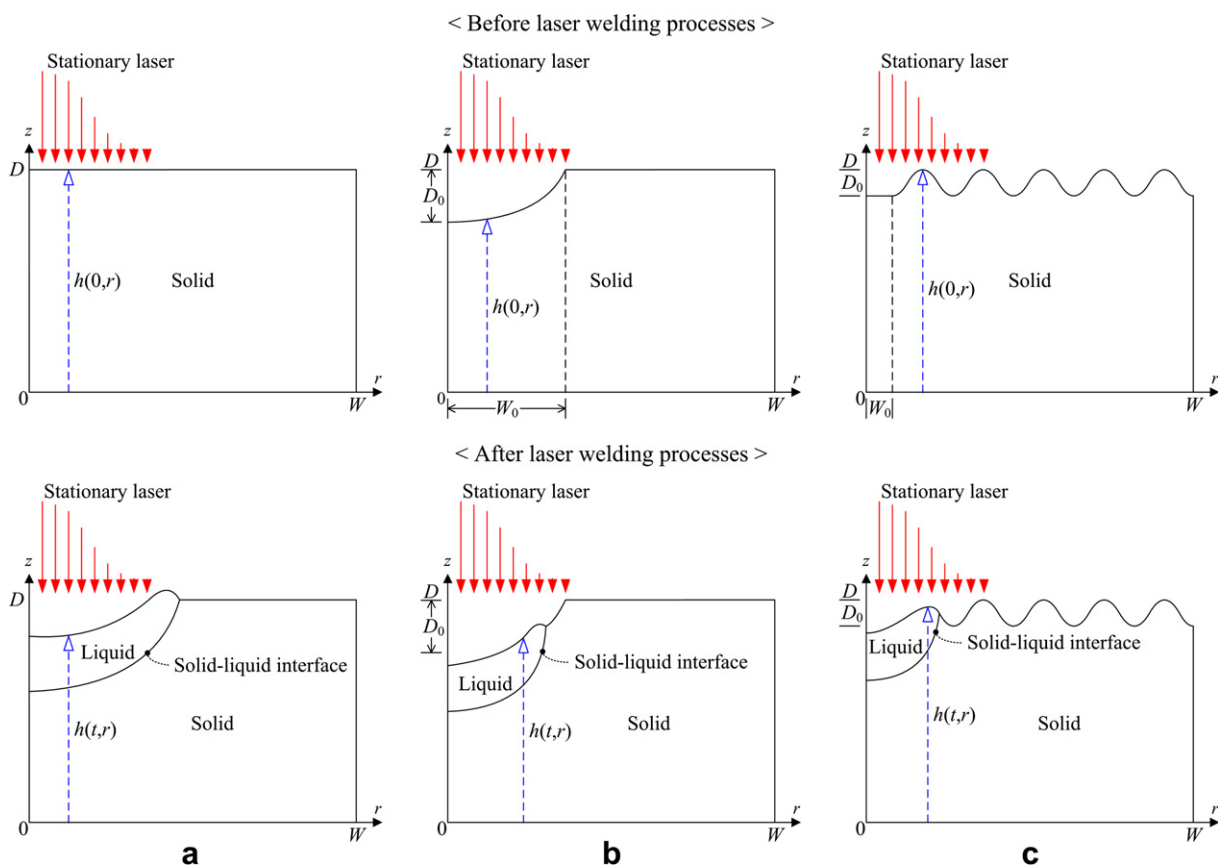

Fig. 1. Schematic illustration of the physical system: (a) flat free surface; (b) parabolic free surface, and (c) sinusoidal wavy free surface.

of an opaque material. Much of the incident radiation is reflected by the heating surface while the rest is absorbed by the base material, which raises the temperature of the target surface above the melting point. Accordingly, the heat absorbed develops a melt pool and the fluid flow in the molten pool is driven primarily by the spatial variation in the surface tension of the molten pool surface. This variation is caused by the large temperature gradient.

The main assumptions adopted for the model are summarized as follows:

1. The laser beam is stationary and continuous, and the heat flux from the laser to the heating surface is a specified symmetric Gaussian distribution.
2. Heat transfer and fluid flow in the molten pool are described by a two-dimensional axisymmetric time-dependent representation, and fluid flow is laminar and incompressible.
3. Thermophysical properties are constant, except for temperature-dependent surface tension.
4. The buoyancy force in the fluid during laser melting is negligible (Srinivasan and Basu, 1986).
5. The top surface outside the beam is adiabatic.

The non-dimensional governing equations for incompressible fluid flow with negligible body forces and heat transfer in the melt pool are defined as follows:

$$\nabla \cdot \mathbf{v} = 0 \tag{1}$$

$$\frac{1}{Ma}\frac{\partial \mathbf{v}}{\partial t} + \nabla \cdot (\mathbf{v}\mathbf{v}) = -\nabla P + \frac{1}{Re}\nabla^2 \mathbf{v} \tag{2}$$

$$\frac{\partial H}{\partial t} + Ma\nabla \cdot (\mathbf{v}H) = \nabla \cdot (k\nabla T) \tag{3}$$

where $\mathbf{v}$, Ma, t, P, Re, H, and k are the velocity vector, the Marangoni number ($Ma = Pr \cdot Re$), time, pressure, the Reynolds number ($Re = U_R \cdot r_b/v$), enthalpy, and the thermal conductivity, respectively, in which Pr, U_R, r_b, and v are the Prandtl number ($Pr = v/\alpha$), surface tension reference velocity ($U_R = \gamma L/C_p\mu$), radius of the laser beam, and the kinematic viscosity, respectively. α, L, γ, C_p, and μ are the thermal diffusivity, latent heat of fusion, the temperature coefficient of surface tension ($\gamma = \partial\sigma/\partial T$), specific heat, and the dynamic viscosity, respectively. σ is the surface tension. Surface tension is assumed to be a linear function of temperature given by

$$\sigma = \sigma_m - \gamma(T^* - T_m), \tag{4}$$

where σ_m, T^*, and T_m are the surface tension at the melting temperature, dimensional temperature, and the melting temperature, respectively.

The boundary conditions for solving the governing equations are as follows:

(i) At the axisymmetrical axis, $r = 0$

$$\frac{\partial T}{\partial r} = u = \frac{\partial v}{\partial r} = 0 \quad \text{for } 0 \leqslant z \leqslant h(t,0) \tag{5}$$

where T, r, u, v, z, and $h(t,r)$ are temperature, the coordinate in the radial direction, the radial velocity, the axial velocity, the coordinate in the axial direction, and the non-dimensional height of the free surface, respectively.

(ii) At the outer surface, $r = W$

$$T = -Ste, \quad u = v = 0 \quad \text{for } 0 \leqslant z \leqslant h(t,W) \tag{6}$$

where W is the radius of the workpiece and Ste is the Stefan number ($Ste = C_p(T_m - T_\infty)/L$), in which T_∞ is the ambient temperature ($T_\infty = 300K$).

(iii) At the bottom surface, $z = 0$

$$T = -Ste, \quad u = v = 0 \quad \text{for } 0 \leqslant r \leqslant W \tag{7}$$

(iv) At the top surface, $z = h(t,r)$

The thermal, kinematic, tangential and normal stress balance boundary conditions at the gas–liquid interface are defined as follows:

$$\frac{1}{N}\left(-h'\frac{\partial T}{\partial r} + \frac{\partial T}{\partial z}\right)$$
$$= \begin{cases} B_f & \text{for } 0 \leqslant r \leqslant 1, \text{ uniform heat flux distribution} \\ B_f(r) & \text{for } 0 \leqslant r \leqslant 1, \text{ Gaussian heat flux distribution} \\ 0 & \text{for } 1 < r \leqslant W \end{cases} \tag{8}$$

$$v = \frac{1}{Ma}\frac{\partial h}{\partial t} + h'u \quad \text{for } 0 \leqslant r \leqslant r_{max} \tag{9}$$

$$(1 - h'^2)\left(\frac{\partial u}{\partial z} + \frac{\partial v}{\partial r}\right) + 2h'\left(\frac{\partial v}{\partial z} - \frac{\partial u}{\partial r}\right)$$
$$= -N\left(\frac{\partial T}{\partial r} + h'\frac{\partial T}{\partial z}\right) \quad \text{for } 0 \leqslant r \leqslant r_{max} \tag{10}$$

$$-Re \cdot P + \frac{2}{N^2}\left[\frac{\partial v}{\partial z} + h'^2\frac{\partial u}{\partial r} - h'\left(\frac{\partial v}{\partial r} + \frac{\partial u}{\partial z}\right)\right]$$
$$= \frac{1 - Ca \cdot T}{Ca \cdot N}\left(\frac{h''}{N^2} + \frac{h'}{r}\right) \quad \text{for } 0 \leqslant r \leqslant r_{max} \tag{11}$$

where $N = (1 + h'^2)^{1/2}$, $h' = \partial h/\partial r$, and B_f is the boundary heating factor ($B_f = q''r_bC_p/k_1L$), in which q'' is the power density of the laser beam, k_1 is the thermal conductivity of the liquid phase, r_{max} and Ca are the maximum radius of the molten pool and the capillary number ($Ca = \gamma L/\sigma_m C_p$), respectively. As shown in Eq. (11), the free surface curvature is determined by both surface pressure and normal viscous stresses.

The energy flux density absorbed by the workpiece surface is determined according to a specified symmetric Gaussian distribution and is given by

$$B_f(r) = \frac{r_bC_p}{k_1L}\frac{3\phi Q}{\pi r_b^2}\exp(-3r^2) \tag{12}$$

where ϕ is the absorption coefficient, and Q is the laser power. The absorption coefficient, ϕ, is influenced by the nature of the surface state and the surface temperature. In the present study, ϕ takes a value of 0.15.

The initial and boundary conditions for solving Eq. (11) are

$$h(0,r) = D \text{ for flat surface}$$
$$= \begin{cases} \frac{D_0}{W_0^2}r^2 + D_1 & \text{for } 0 \leqslant r < W_0 \\ D & \text{for } W_0 \leqslant r \leqslant W \end{cases} \text{ for parabolic surface}$$
$$= \begin{cases} D_1 & \text{for } 0 \leqslant r < W_0 \\ D_1 + A\left\{1 + \sin\left[\frac{2\pi}{\lambda}\left(r - D_0 - \frac{0.25}{\lambda}\right)\right]\right\} & \text{for } W_0 \leqslant r \leqslant W \end{cases} \text{ for sinusoidal wavy surface}$$

$$h'(t,0) = 0$$
$$h(t, r_{max}) = h(0, r_{max}) \tag{13}$$

where $D_1 = D - D_0$, $\lambda = (W - W_0)/m$, in which m is the non-dimensional wave number. In the present study, m is 5. For a parabolic free surface, $D_0 = 0.1$ or 0.2 and $W_0 = 1$ while for a sinusoidal wavy surface, $D_0 = 0.1$ and $W_0 = 0.25$.

Since the total volume of the molten pool is assumed to be the same as the original base metal, its changed total volume must be zero as follows:

$$V = \int_0^{r_{max}} [h(t,r) - h(0,r)] r \, dr = 0 \tag{14}$$

where V is the non-dimensional liquid volume. The equations mentioned above are non-dimensionalized by the following dimensionless variables:

$$t = \frac{t^* \alpha}{r_b^2}, \quad r = \frac{r^*}{r_b}, \quad \mathbf{v} = \frac{\mathbf{v}^*}{U_R}, \quad P = \frac{P^*}{\rho U_R^2},$$
$$T = \frac{C_p(T^* - T_m)}{L}, \quad k = \frac{k^*}{k_1}$$

where ρ is the density. The superscript * denotes the dimensional variables.

3. Numerical model description

3.1. Numerical model

In order to solve the laser melting problem with a deformable surface, the physical domain (t,r,z) must be transformed into a rectangular computational domain (t,ξ,η) before a standard finite volume method can be applied to the solution of the governing differential equations discussed above.

$$\xi = r, \quad \eta = \frac{zD}{h(t,r)} \tag{15}$$

The transformed governing equations are as follows:

$$\frac{1}{\xi} \frac{\partial \xi u}{\partial \xi} - \eta \frac{h'}{h} \frac{\partial u}{\partial \eta} + \frac{D}{h} \frac{\partial v}{\partial \eta} = 0 \tag{16}$$

$$\frac{1}{Ma}\left[\frac{\partial u}{\partial t} - \frac{\eta}{h} \frac{\partial h}{\partial t} \frac{\partial u}{\partial \eta} \right] + \frac{1}{\xi} \frac{\partial \xi u^2}{\partial \xi} - \eta \frac{h'}{h} \frac{\partial u^2}{\partial \eta} + \frac{D}{h} \frac{\partial uv}{\partial \eta}$$
$$= -\frac{\partial P}{\partial \xi} + \eta \frac{h'}{h} \frac{\partial P}{\partial \eta} + \frac{1}{Re}\left[\nabla^2 u - \frac{u}{\xi^2} \right] \tag{17}$$

$$\frac{1}{Ma}\left[\frac{\partial v}{\partial t} - \frac{\eta}{h} \frac{\partial h}{\partial t} \frac{\partial v}{\partial \eta} \right] + \frac{1}{\xi} \frac{\partial \xi uv}{\partial \xi} - \eta \frac{h'}{h} \frac{\partial uv}{\partial \eta} + \frac{D}{h} \frac{\partial v^2}{\partial \eta} = -\frac{D}{h} \frac{\partial P}{\partial \eta} + \frac{1}{Re} \nabla^2 v \tag{18}$$

$$\frac{\partial T}{\partial t} - \frac{\eta}{h} \frac{\partial h}{\partial t} \frac{\partial T}{\partial \eta} + Ma\left[\frac{1}{\xi} \frac{\partial \xi uT}{\partial \xi} - \eta \frac{h'}{h} \frac{\partial uT}{\partial \eta} - \frac{D}{h} \frac{\partial vT}{\partial \eta} \right]$$
$$= \frac{1}{\xi} \frac{\partial}{\partial \xi}\left(k\xi \frac{\partial T}{\partial \xi} \right) - \frac{\eta h'}{h}\left[\frac{\partial}{\partial \eta}\left(k\frac{\partial T}{\partial \xi} \right) + \frac{\partial}{\partial \xi}\left(k\frac{\partial T}{\partial \eta} \right) \right]$$
$$+ \left[2\left(\frac{h'}{h}\right)^2 - \frac{h''}{h} - \frac{h'}{h\xi} \right]\eta k \frac{\partial T}{\partial \eta} + \left[\left(\frac{h'\eta}{h}\right)^2 + \frac{D^2}{h^2} \right]\frac{\partial}{\partial \eta}\left(k\frac{\partial T}{\partial \eta} \right) - \frac{\partial f}{\partial t} \tag{19}$$

$$\nabla^2 = \frac{1}{\xi} \frac{\partial}{\partial \xi}\left(\xi \frac{\partial}{\partial \xi} \right) - \frac{2\eta h'}{h} \frac{\partial^2}{\partial \eta \partial \xi} + \left[2\left(\frac{h'}{h}\right)^2 - \frac{h'}{h} - \frac{h'}{h\xi} \right]\eta \frac{\partial}{\partial \eta}$$
$$+ \left[\left(\frac{\eta h'}{h}\right)^2 + \frac{D^2}{h^2} \right]\frac{\partial^2}{\partial \eta^2} \tag{20}$$

where f denotes the local liquid fraction. In the energy Eq. (19), the latent heat of fusion is associated with the liquid fraction, f, which is defined as follows (Swaminathan and Voller, 1993):

$$f = 1 \quad \text{for } T \geqslant T_m \tag{21}$$
$$f = 0 \quad \text{for } T < T_m \tag{22}$$

In addition, the transformed boundary conditions are given as

At $\xi = 0$, $\quad \frac{\partial T}{\partial \xi} = u = \frac{\partial v}{\partial \xi} = 0 \quad \text{for } 0 \leqslant \xi \leqslant D \tag{23}$

At $\xi = W$, $\quad T = -Ste, \quad u = v = 0 \quad \text{for } 0 \leqslant \xi \leqslant D \tag{24}$

At $\eta = 0$, $\quad T = -Ste, \quad u = v = 0 \quad \text{for } 0 \leqslant \xi \leqslant W \tag{25}$

At $\eta = D$,

$$\frac{D(1 + h'^2)}{h} \frac{\partial T}{\partial \eta} - h' \frac{\partial T}{\partial \xi}$$
$$= \begin{cases} N \cdot B_f & \text{for } 0 \leqslant \xi \leqslant 1, \text{ uniform heat flux distribution} \\ N \cdot B_f(\xi) & \text{for } 0 \leqslant \xi \leqslant 1, \text{ Gaussian heat flux distribution} \\ 0 & \text{for } 1 < \xi \leqslant W \end{cases} \tag{26}$$

$$v = \frac{1}{Ma} \frac{\partial h}{\partial t} + h'u \quad \text{for } 0 \leqslant \xi \leqslant \xi_{max} \tag{27}$$
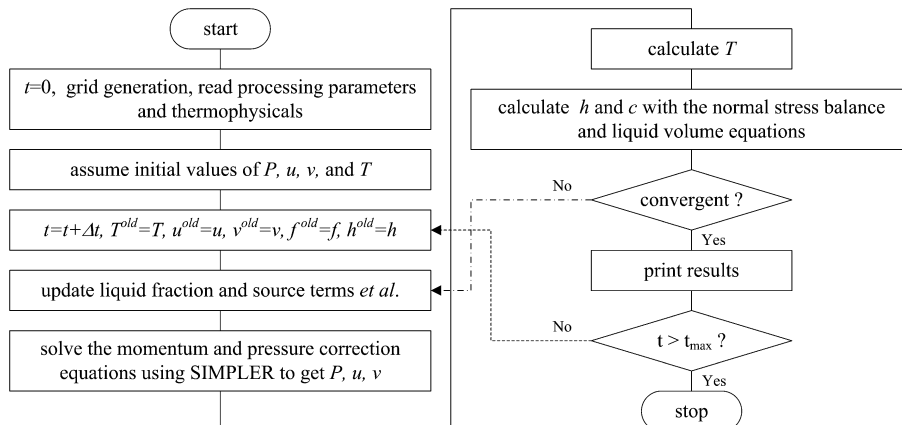

Fig. 2. Flow chart of calculation. The superscript expresses the value of the previous time increment.

$$D\left(\frac{1+h'^2}{h}\right)\frac{\partial u}{\partial \eta} - 2h'\frac{\partial u}{\partial \xi} + \left(\frac{h'+h'^3}{h}\right)\frac{\partial v}{\partial \eta} + (1-h'^2)\frac{\partial v}{\partial \xi}$$

$$= -N\frac{\partial T}{\partial \xi} \quad \text{for } 0 \leqslant \xi \leqslant \xi_{max} \tag{28}$$

$$-Re \cdot P + \frac{2D}{h}\left(\frac{\partial v}{\partial \eta} - h'\frac{\partial u}{\partial \eta}\right) + \frac{2h'}{N^2}\left(h'\frac{\partial u}{\partial \xi} - \frac{\partial v}{\partial \xi}\right)$$

$$= \frac{1 - Ca \cdot T}{Ca \cdot N}\left(\frac{h''}{N^2} + \frac{h'}{\xi}\right) \quad \text{for } 0 \leqslant \xi \leqslant \xi_{max} \tag{29}$$

The transformed equations of Eqs. (12)–(14) are as follows:

$$B_f(\xi) = \frac{r_b C_p}{k_1 L}\frac{3\phi Q}{\pi r_b^2}\exp(-3\xi^2) \tag{30}$$

$$h(0,\xi) = D \text{ for flat surface}$$

$$= \begin{cases} \frac{D_0}{W_0^2}\xi^2 + D_1 & \text{for } 0 \leqslant \xi < W_0 \\ D & \text{for } W_0 \leqslant \xi \leqslant W \end{cases} \text{ for parabolic surface}$$

$$= \begin{cases} D_1 & \text{for } 0 \leqslant \xi < W_0 \\ D_1 + A\left\{1 + \sin\left[\frac{2\pi}{\lambda}\left(\xi - D_0 - \frac{0.25}{\lambda}\right)\right]\right\} & \text{for } W_0 \leqslant \xi \leqslant W \end{cases} \text{ for sinusoidal wavy surface} \tag{31}$$

$$h'(t,0) = 0$$

$$h(t,\xi_{max}) = h(0,\xi_{max})$$

$$V = \int_0^{\xi_{max}} [h(t,\xi) - h(0,\xi)]\xi \, d\xi = 0 \tag{32}$$

3.2. Numerical algorithm

The transformed governing Eqs. (16)–(19) and boundary conditions, Eqs. (23)–(29), are discretized using the control volume ap-

Table 1
Thermophysical properties of steel and input parameters for simulation (Ravindran et al., 1994)

Variable	Value	Variable	Value
ρ	7200 kg/m³	C_p	753 J/kgK
k_s	31.39 W/mK	k_1	15.48 W/mK
μ	0.006 Ns/m²	L	2.47×10^5 J/kg
T_m	1723 K	r_b	1 mm
Pr	0.292	Ste	4.338
Process parameters			
Re [γ]	65.6 [-10^{-6} N/mK], 656 [-10^{-5} N/mK], 6560 [-10^{-4} N/mK]		
$B_f(0)$ [Q]	22.57 [800 W], 25.39 [900 W], 28.21 [1000 W]		

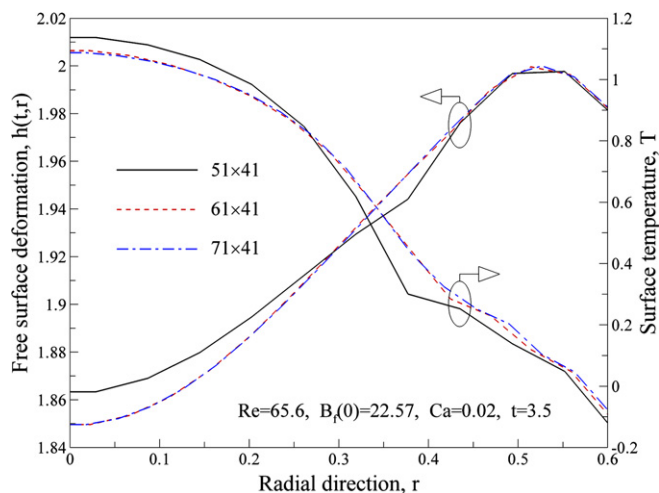proach in the transformed domain, which results in the following equation:

$$a_P \Phi_P = a_E \Phi_E + a_W \Phi_W + a_T \Phi_T + a_B \Phi_B + S \tag{33}$$

where Φ stands for each variable (u, v, T, P, and $h(t,r)$). The values of a_P, a_E, a_W, a_T, and a_B are the coefficients obtained from Eqs. (16)–(19) and Eqs. (23)–(29), and S is the source term.

Governing Eqs. (16)–(19), in conjunction with the boundary conditions, Eqs. (23)–(29), are solved by using a finite volume method employing a SIMPLER algorithm. In normal stress balance boundary conditions, Eq. (29), the variable P contains a free integration constant, $c(t)$, and the free surface shape, $h(t,r)$, and $c(t)$


Fig. 3. Grid refinement studies for the sinusoidal wavy free surface with $Re = 65.6$, $B_f(0) = 22.57$, and $Ca = 0.02$ at $t = 3.5$. The values of D_0 and W_0 are 0.1 and 0.25, respectively.
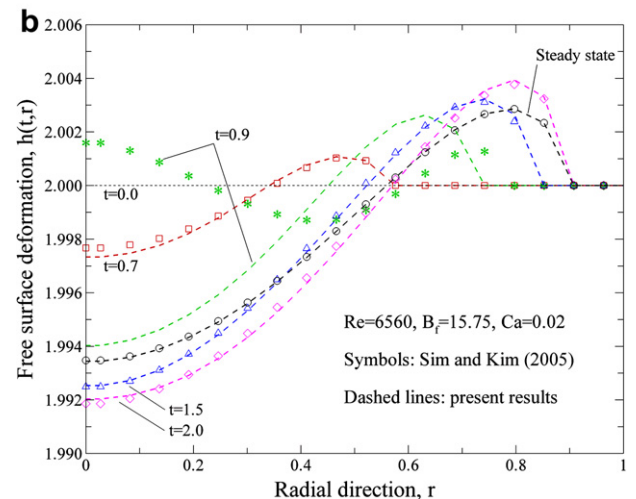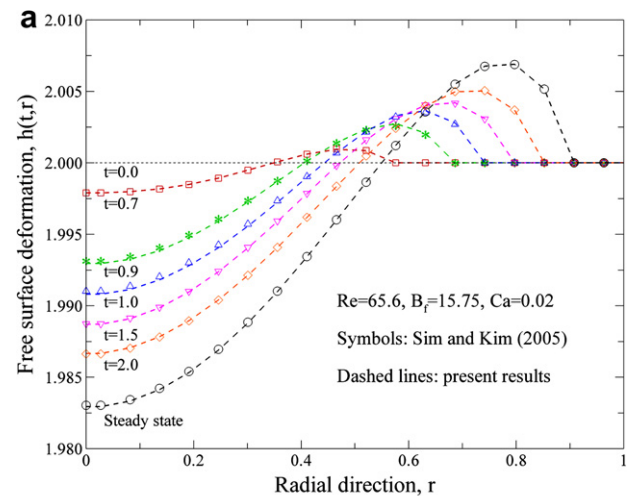

Fig. 4. Transient surface deformation for $B_f = 15.75$ (uniform heat flux distribution) and $Ca = 0.02$ with a flat free surface. The data (symbols) of Sim and Kim (2005) are shown and compared to the computed data (lines): (a) $Re = 65.6$ and (b) $Re = 6560$.
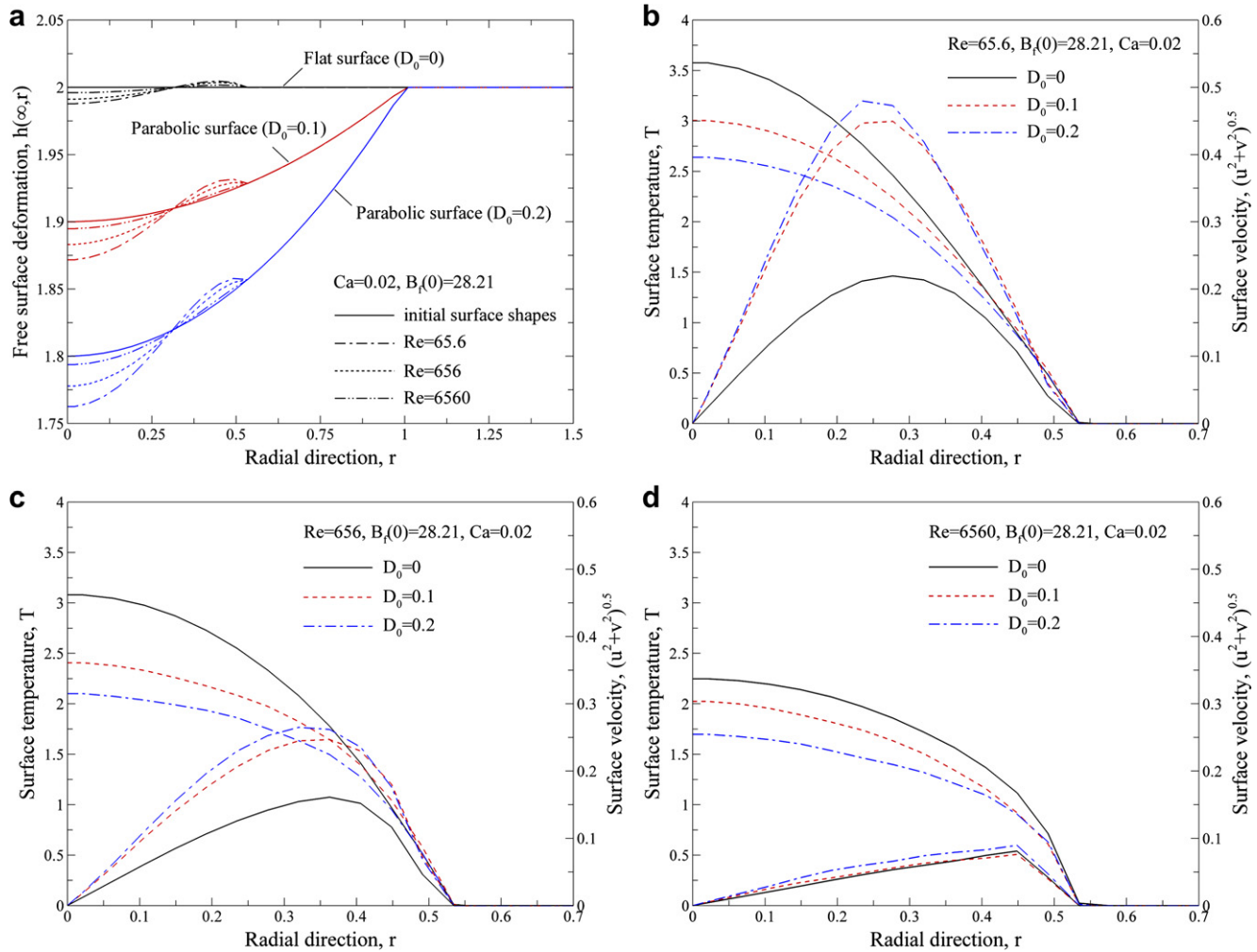
Fig. 5. Free surface profiles, surface temperature and velocity distributions of a molten pool with $B_f(0) = 28.21$, $Ca = 0.02$, and various Re for flat and parabolic surface shapes: (a) surface deformation; (b) $Re = 65.6$; (c) $Re = 656$, and (d) $Re = 6560$.
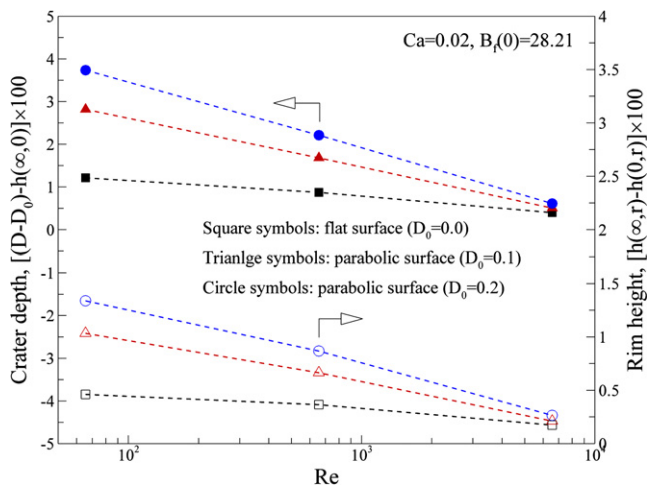
Fig. 6. Free surface deformations with respect to Re at $Ca = 0.02$ and $B_f(0) = 28.21$ for flat and parabolic surfaces.

are determined by using Eqs. (29), (31), and (32) (Sim and Kim, 2005). To obtain a free integration constant, $c(t)$, each time, Broyden's method, which is a quasi-Newtonian method for numerical solution of non-linear equations, is used (Broyden, 1965). A non-uniform grid system with denser grids in the region adjacent

to the molten pool is used in this study. A numerical iteration procedure is summarized in Fig. 2. Convergence for steady-state is declared if the following condition is satisfied at each grid point:

$$\left| \frac{\Phi^{n+1} - \Phi^n}{\Phi^{n+1}} \right| \leqslant 10^{-3} \tag{34}$$

where n represents the time iteration level.

The material properties and other information pertaining to the simulation are given in Table 1. The 51×41, 61×41, and 71×41 grid systems are used to examine the grid dependency and free surface deformations. Surface temperature distributions with various grids are compared in Fig. 3. The differences in surface temperatures and surface deformations between 61×41 and 71×41 grid sizes are very small. However, the maximum errors in the surface temperatures and deformations for the 51×41, 61×41, and 71×41 grid systems are approximately 51% and 0.74%, respectively. Accordingly, the model uses the 61×41 grid size for numerical calculation.

4. Results and discussion

### 4.1. Validation of numerical algorithm

Fig. 4 compares the predicted surface deformation to that of Sim and Kim (2005). The deformation predicted by Sim and Kim (2005)

shows very good agreement with numerical and experimental results previously published in the literature. Here, the 41 × 41 grid size is used to analyze the laser melting process with a deformable flat surface with the same simulation conditions as Sim and Kim (2005). As shown in Fig. 4, the predicted surface deformations are remarkably consistent with those of Sim and Kim (2005), except for the surface deformation profile for $Re = 6560$ at $t = 0.9$.

For the case of $Re = 6560$, Sim and Kim (2005) suggested that two kinds of surface shapes in the laser melting of steel are formed with time, bowl and sombrero-shaped bumps. However, as mentioned before (Chen et al., 2000), the formation mechanism of a sombrero bump during pulsed laser melting of a Ni–P substrate is explained by the competition between thermocapillary and concentration-induced capillary effects. Therefore, the surface

Table 2
Effect of Re, Ca, and B_f on the molten pool with flat and parabolic surfaces

Parameters	Values	Flat surface ($D_0 = 0$)			Parabolic surface					
					($D_0 = 0.1$)			($D_0 = 0.2$)		
		Width	Depth	T_{max}	Width	Depth	T_{max}	Width	Depth	T_{max}
Re	65.6	0.534	0.174	3.576	0.534	0.147	3.005	0.534	0.123	2.641
[$Ca = 0.02$,	656	0.534	0.157	3.080	0.534	0.132	2.408	0.534	0.110	2.102
$B_f(0) = 28.21$]	6560	0.534	0.123	2.248	0.534	0.117	2.024	0.534	0.096	1.697
Ca	0.01	0.534	0.175	3.669	0.534	0.166	3.297	0.534	0.140	2.874
[$Re = 65.5$,	0.02	0.534	0.174	3.576	0.534	0.147	3.005	0.534	0.123	2.641
$B_f(0) = 28.21$]	0.03	0.534	0.174	3.453	0.534	0.147	2.963	0.534	0.123	2.547
$B_f(0)$	22.57	0.406	0.107	2.004	0.406	0.101	1.836	0.363	0.083	1.515
[$Re = 65.5$,	25.39	0.449	0.139	2.788	0.449	0.132	2.500	0.449	0.096	1.959
$Ca = 0.02$]	28.21	0.534	0.174	3.576	0.534	0.147	3.005	0.534	0.123	2.641
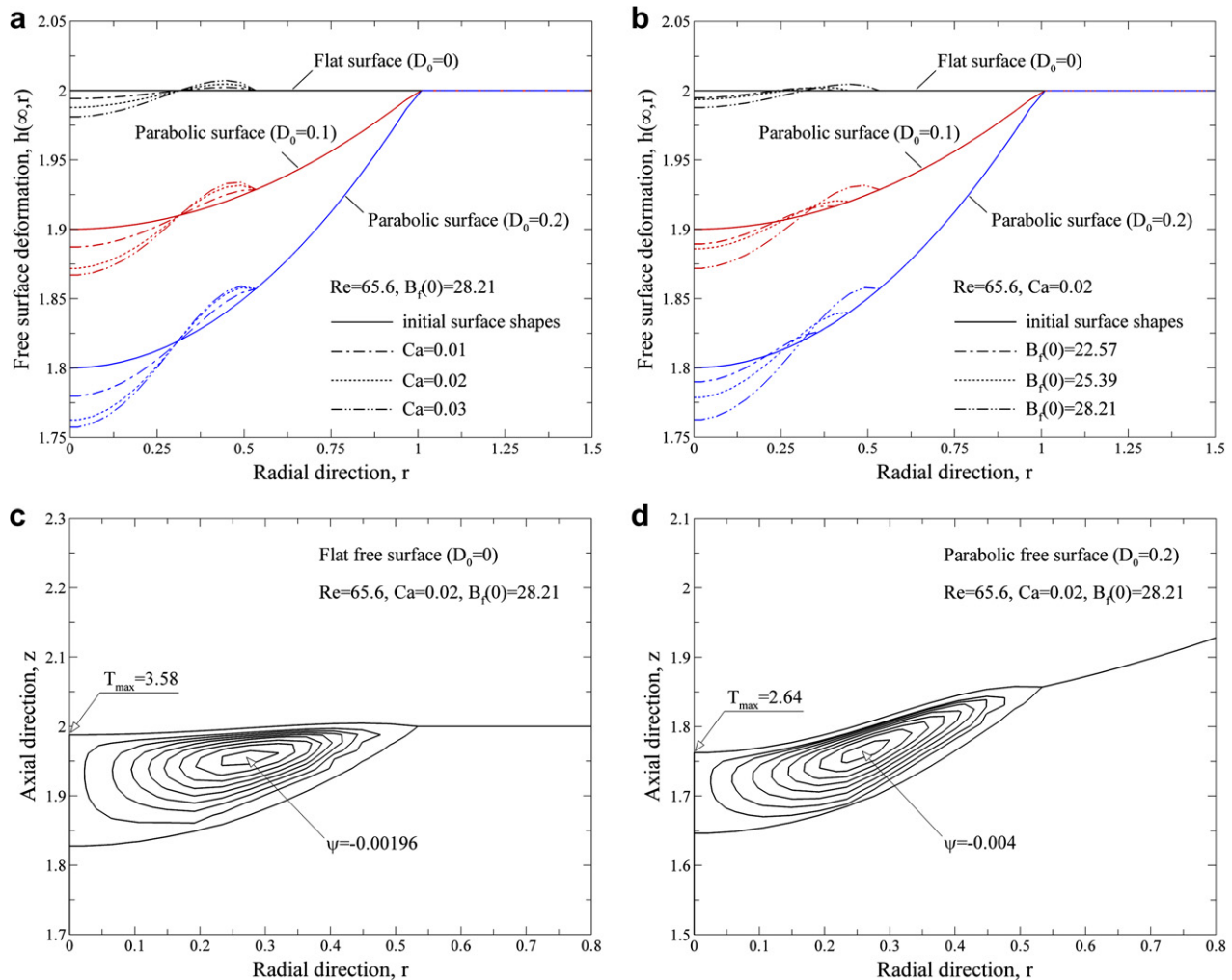
Fig. 7. Free surface profiles of molten pool with $Re = 65.6$ and various Ca and B_f, and streamlines with $Re = 65.6$, $Ca = 0.02$, and $B_f (0) = 28.21$ for flat and parabolic surface shapes: (a) Ca; (b) B_f; (c) flat free surface, and (d) parabolic free surface with $D_0 = 0.2$.

chemistry in the theoretical analysis of Ni–P, unlike that of steel, has to be considered to accurately predict the bump formation process of Ni–P substrates with pulsed laser melting. As mentioned above, the present results are reasonable compared with those of Sim and Kim (2005).

As shown in Fig. 4, the bump has a deep crater at the center and a low peripheral rim with a bowl-like shape, at both low and high Re. Over time, the crater diameter increases and deepens, and the rim height increases and widens due to enhanced thermocapillary convection at a low Re number (65.6). At a high Re, the surface deformation decreases over time after attaining a maximum value at $t = 2$, which is because the driving force in the molten material from the hot center to the cold periphery is smaller at a high Re than at a low Re.

4.2. Steady-state analysis of laser melting process

In this case, numerical calculation has been performed to examine how the shape, size, and surface topography of the molten pool during steady laser surface melting are affected by the curved surface shape (h), surface tension force (Re), laser power intensity (B_f), and the ratio of the viscous force to the surface tension force (Ca).

4.2.1. Thermocapillary convection for flat and parabolic surfaces

Fig. 5 illustrates the surface topographies, surface temperature and velocity profiles of a molten pool with $B_f(0) = 28.21$, $Ca = 0.02$, and various Re for flat and parabolic surface shapes.

The free surface is concave ("crater") at the hot center and convex ("rim") near the cold periphery, because the surface temperature gradient-induced thermocapillary flow drives the molten material towards the cooler region with higher surface tension. As shown in Fig. 5a, the shape of the surface, number of ripples, and reflection point are not qualitatively affected by Re and the curvature of the free surface. As Re increases, the surface temperature gradient and hence the surface velocity decreases as shown in Fig. 5b–d. The maximum temperature and velocity increase with decreasing Re. The increased velocities induce larger surface deformations at a fixed Ca and B_f. As the curvature of the free surface increases at the same Re, while the surface temperature gradient decreases, the surface velocity increases greatly. The effect of the curvature of the free surface is very small at the higher Re indicating stronger surface tension force. Thus, the surface deformations increase gradually with decreasing Re due to vigorous thermocapillary convection and increase monotonically with increasing curvature of the free surface. That is, flows with concave free surfaces tend to be faster than those of flat surfaces for two reasons. One is that the average flow passage is narrower (see Fig. 7c and d), which increases the surface velocity (see Fig. 5b–d); and the other is that the thermocapillary flow is enhanced with larger inertia effect of upward molten material flow compared to the flat surface when the flow direction is concerned. It becomes more effective in driving the flow cell. As shown in Fig. 7c and d, it can be seen that the maximum value of the stream functions with parabolic free surface is almost twice as large as that of the flat surface. The flow characteristics of thermocapillary convection with a flat and curved surface can be found in Sim and Zebib (2002) and Sim et al. (2004).

Fig. 6 shows the depth of the crater and height of the peripheral rim as a function of Re. As mentioned before, the curvature, shape (convex or concave), and magnitude of the free surface is determined by both the surface pressure and normal viscous stresses, as shown in Eq. (29). The effect of the surface pressure on surface deformation is more significant at the lower Re, while the viscous stresses become dominant with increasing Re, which leads to a small deformation in the free surface. At a lower Re the effect of the curvature of the free surface on the surface deformation is

large, while its effect is negligibly small at a higher Re. This indicates a stronger surface tension force at fixed Ca and B_f. The orders of magnitude of surface deformation, the crater depth and rim height, are the same as $O(10^{-3})$, and their maximum values are 3.74×10^{-2} and 1.34×10^{-2}, respectively, with $Re = 65.6$ and a parabolic surface in which $D_0 = 0.2$. As shown in Table 2, the width of the pool is almost independent of Re and the curvature of the free surface, while the depth decreases with an increase in Re and the curvature of the free surface.

Fig. 7 shows the free surface variations in a molten pool at steady-state with respect to Ca and B_f at $Re = 65.5$, and the streamlines in the molten pool for flat and parabolic surface shapes. The value of the capillary number is in the range $1.69 \times 10^{-4} \leqslant Ca \leqslant 1.69 \times 10^{-2}$ with $-10^{-6} \leqslant \gamma \leqslant -10^{-4}$ and $\sigma_m = 1.943$ N/m (Fan et al., 2001; Sim and Kim, 2005). It is a well-known fact that the surface deformations can be neglected as the capillary number approaches zero, indicating a very high surface tension. As depicted in Fig. 7a, the depth of the crater and rim height increase simultaneously with increasing Ca due to low surface tension and the curvature of the free surface; the shape of the surface, number of ripples, and reflection point do not qualitatively change with Ca at fixed Re and B_f. Fig. 8 denotes the free
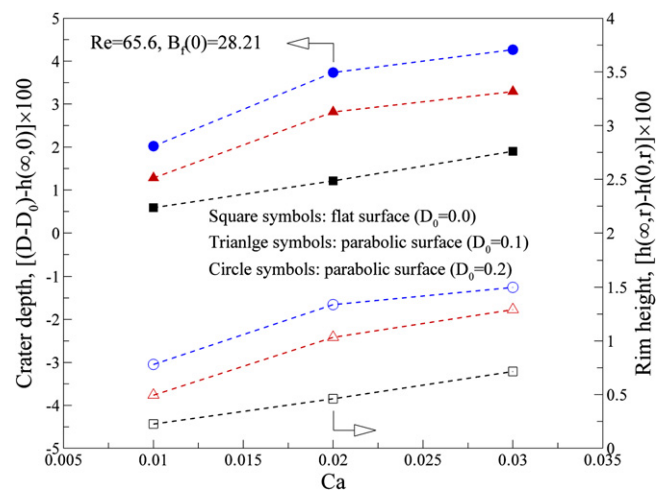

Fig. 8. Free surface deformations with respect to Ca with $Re = 65.5$ and $B_f(0) = 28.21$ for flat and parabolic surfaces.
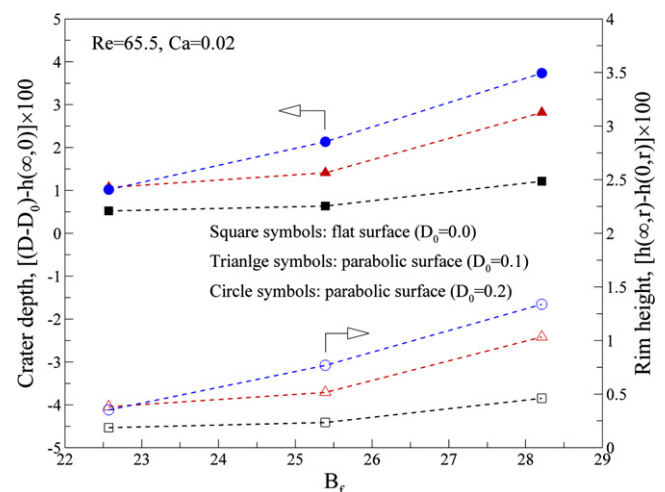

Fig. 9. Free surface deformations with respect to B_f at $Re = 65.5$ and $Ca = 0.02$ for flat and parabolic surfaces.

surface deformations with variations in the surface shapes and Ca. It can be seen that the curvature of the free surface has a substantial effect on the surface deformation regardless of Ca, which has little effect on the convection (Sim et al., 2004), unlike the effects of Re and B_f shown in Figs. 6 and 9. The orders of magnitude of the crater depth and rim height are also the same as $O(10^{-3})$,

and their maximum values are 4.27×10^{-2} and 1.5×10^{-2}, respectively, with $Ca = 0.03$ and a parabolic surface with $D_0 = 0.2$. When the curvature of the free surface and Ca increase, the variations in the pool width are negligibly small, while the depth of the pool decreases slightly, as shown in Table 2.
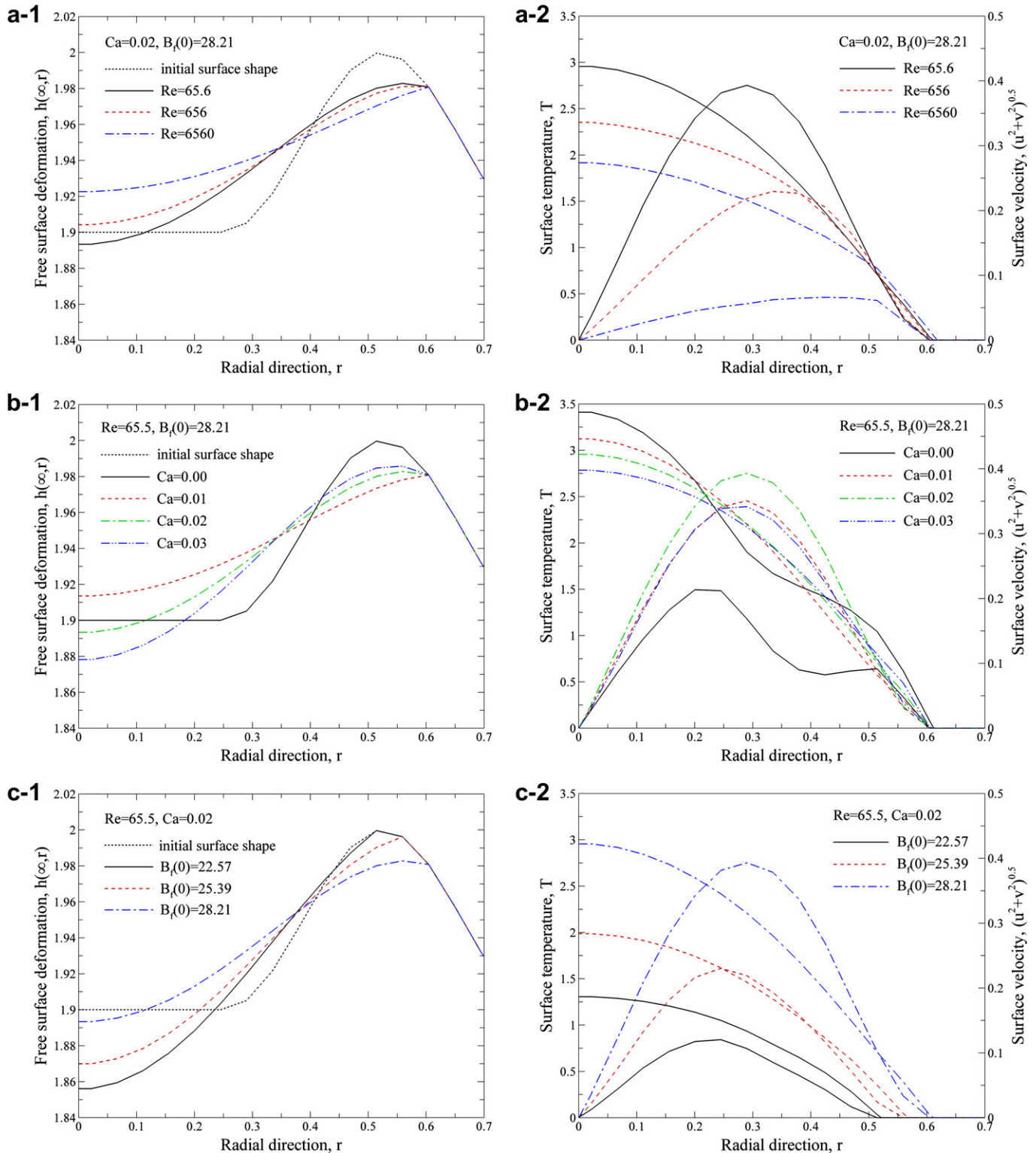
Fig. 10. Effect of Re, Ca, and B_f on the surface deformation, temperature, and velocity distributions of the molten pool with sinusoidal wavy surface: (a) Re with $Ca = 0.02$ and $B_f(0) = 28.21$; (b) Ca with $Re = 65.6$ and $B_f(0) = 28.21$, and (c) B_f with $Re = 65.6$ and $Ca = 0.02$.

As shown in Fig. 7b, as expected, when B_f increases with $Re = 65.5$ and $Ca = 0.02$, the melt pool expands and the crater radius increases and deepens. The rim height keeps increasing and widening due to stronger convection. It is shown that the shape of the surface and the number of ripples, except at a reflection point, are not qualitatively influenced by B_f at fixed Re and Ca. The free surface deformations with respect to the variations in B_f and surface shapes are illustrated in Fig. 9. It can be seen that the curvature of the free surface has very little effect on the surface deformation at a lower B_f, while at a higher B_f it substantially influences the surface deformation at fixed Re and Ca. The depth of the molten pool becomes smaller with an increasing curvature of the free surface at fixed B_f, but its effect on the width is negligibly small, and the width and depth of the molten pool increase with increasing B_f for a fixed surface shape, as shown in Table 2.

Accordingly, the numerical results for flat and curved surfaces described above show that the curvature of the curved free surface has a substantial influence on the shape, size, and surface topography of the weld pool. That is, as the curvature of the free surface increases, the actual pool width along the free surface increases and the depth decreases with the formation of more large bumps because of enhanced thermocapillary flow compared to that of the flat surface. In particular, it is noted that the curvature of the free surface has little effect on the sizes of the crater depth and rim height at a higher Re and lower B_f with fixed Ca. The effect is much stronger at a lower Re and higher B_f, indicating stronger convection, and the curvature of the free surface has a substantial influence on the surface deformation regardless of Ca, unlike the effects of Re and B_f shown in Figs. 6 and 9.
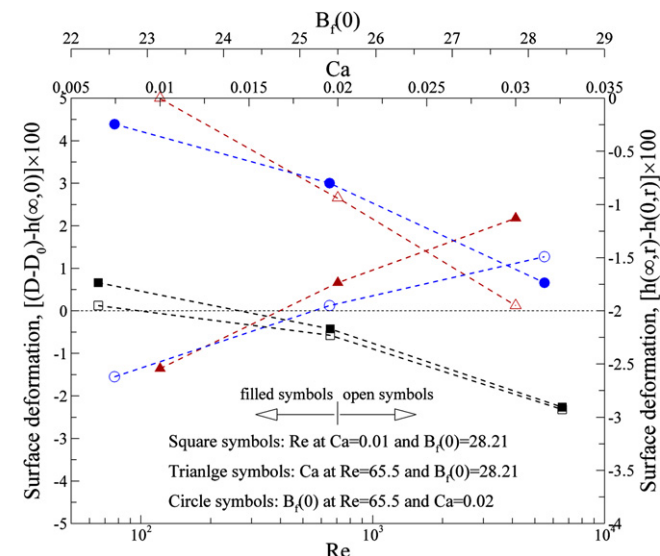
4.2.2. Thermocapillary convection for a sinusoidal wavy surface

Fig. 10a shows free surface variations, and surface temperature and velocity distributions in the molten pool at steady-state with respect to Re when $Ca = 0.02$ and $B_f(0) = 28.21$. As Re increases, the thermocapillary convection becomes weaker, carrying the molten material inward, and causing recovery of the crater center. Therefore, the slope of the crater decreases gradually, as shown in Fig. 10a. In Fig. 11, the plus sign on the vertical axis on the left-hand side shows that the height of the free surface is lower than that of the initial free surface at the center, where the minus sign indicates the opposite.

As Re increases from 65.6 to 6560, as shown in Figs. 10a and 11 and Table 3, the heights of the free surface at the center of the pool decrease by approximately 4.5% of the pool depth, and increase by approximately 3.6% and 22% of the pool depth, respectively, and decrease by approximately 13.1%, 19.1%, and 28.4% at the peak, respectively, compared to that of the initial free surface. In addition, it can be seen that the maximum temperature and velocity decrease dramatically, and the center of the recirculations moves closer to the cold wall with an increase in Re.

Fig. 10b shows variations in the free surface, surface temperature and velocity profiles at steady-state with Ca at a fixed $Re = 65.5$ and $B_f(0) = 28.21$. The crater becomes deeper, as expected, causing an increase in the slope of the crater with a correspondingly increasing Ca indicating low surface tension. As Ca increases from 0.01 to 0.03, the volume of the molten pool increases slightly with increasing the height of the rim, even though the pool depth decreases as shown in Table 3. The volumes of the melt pool are 1.261×10^{-2}, 1.347×10^{-2}, and 1.386×10^{-2} for each Ca. As shown in Fig. 10b-2, when Ca increases from 0 to 0.02, the surface velocity increases greatly due to the effect of the curvature of the free surface as mentioned before. Above $Ca = 0.02$, however, the surface velocity decreases again due to higher kinetic energy loss in the flow, which is induced by abrupt change in flow direction from radial-inward to outward with smaller depth of the molten pool, compared to that of $Ca = 0.02$. However, the variations in Ca have little effect on thermocapillary convection compared to those with Re and B_f. This result is qualitatively consistent with that of an open cylindrical annuli (Sim et al., 2004). The free surface heights at the center increase by about 9% of the pool depth and decrease by about 4.5% and 16.6% of the pool depth, and at the peak decrease by about 17.5%, 13.1%, and 11.4% of the pool depth, compared to that of the initial free surface, as Ca increases from 0.01 to 0.03 as shown in Figs. 10b and 11 and Table 3.

The free surface profiles, surface temperature and velocity distributions of the molten pool for varying B_f with $Re = 65.5$ and $Ca = 0.02$ are shown in Fig. 10c. As expected, the width and depth of the molten pool, surface temperature, and velocity increase remarkably, and the center of the recirculation moves slightly towards the solid–liquid interface with increasing B_f. Although the thermocapillary convection at a higher B_f is much stronger than that at a lower B_f, as B_f increases, the height of the free surface at the center increases along with a decrease in the slope of the crater, which carries large amounts of the molten material inward. Therefore, as B_f increases from 22.57 to 28.21, the heights of the

Fig. 11. Free surface deformations with respect to Re, Ca, and B_f for a sinusoidal wavy surface: the vertical axes at the left- and right-hand sides represent the surface deformation at the center and peak ($r \approx 0.514$), respectively.

Table 3
Effect of Re, Ca, and B_f on the molten pool with a sinusoidal wavy surface

| Melt pool	Re [$Ca = 0.02, B_f(0) = 28.21$]			Ca [$Re = 65.5, B_f(0) = 28.21$]				$B_f(0)$ [$Re = 65.5, Ca = 0.02$]		
	65.6	656	6560	0.00	0.01	0.02	0.03	22.57	25.39	28.21
Width	0.604	0.604	0.604	0.604	0.604	0.604	0.604	0.514	0.559	0.604
Depth	0.149	0.117	0.103	0.167	0.150	0.149	0.131	0.072	0.100	0.149
T_{max}	2.956	2.353	1.916	3.412	3.123	2.956	2.786	1.307	1.987	2.956
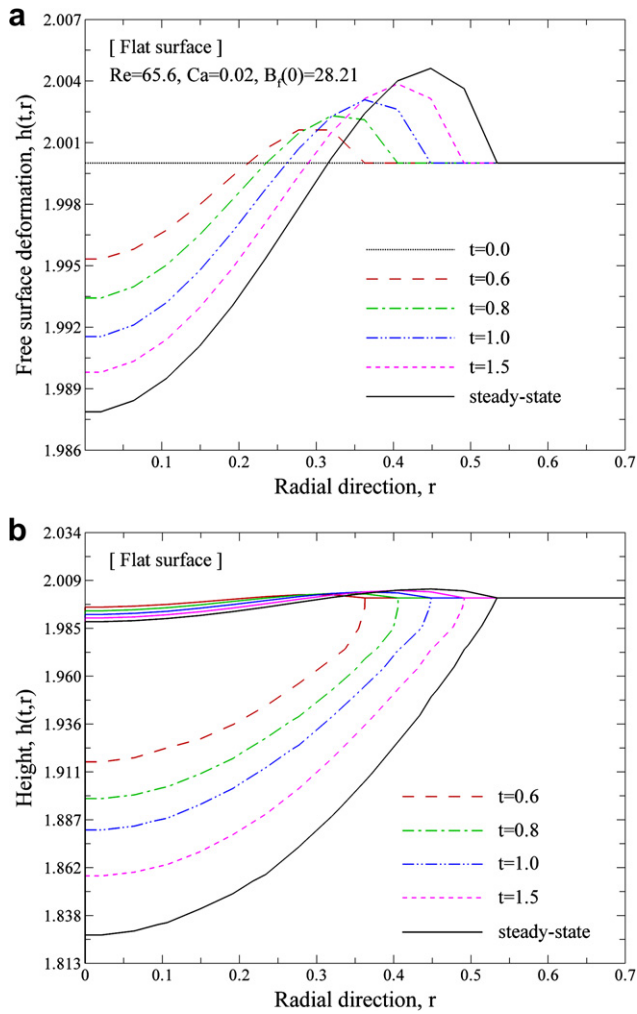
Fig. 12. Transient surface deformation and shape of the molten pool for a flat surface with $Re = 65.6$, $Ca = 0.02$, and $B_f(0) = 28.21$.
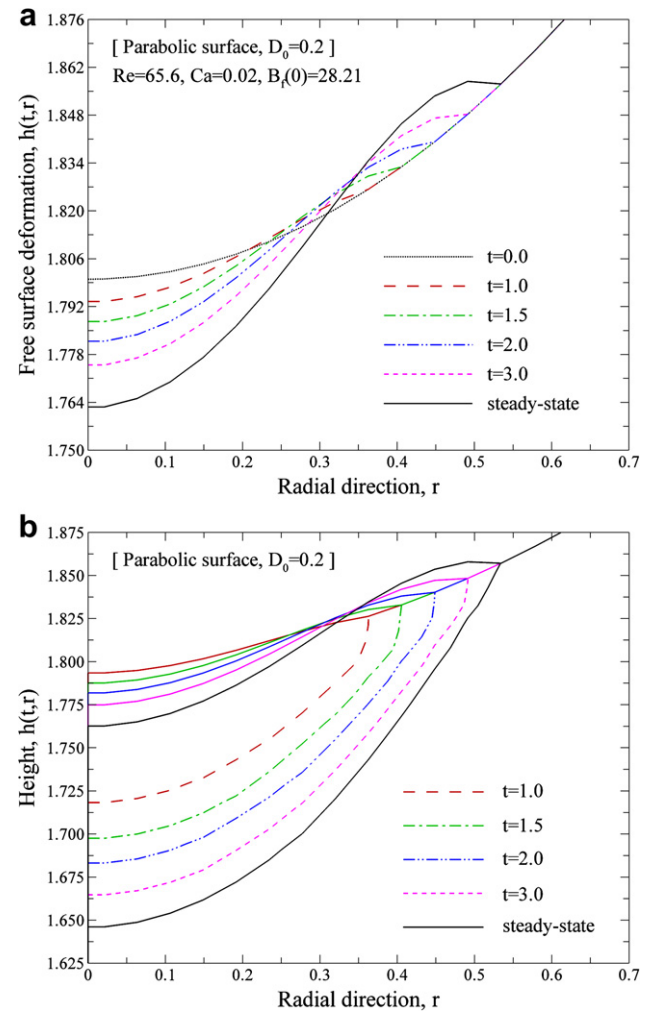
Fig. 14. Transient surface deformation and shape of the molten pool for a parabolic surface with $Re = 65.6$, $Ca = 0.02$, and $B_f(0) = 28.21$. The values of D_0 and W_0 are 0.2 and 1.0, respectively.
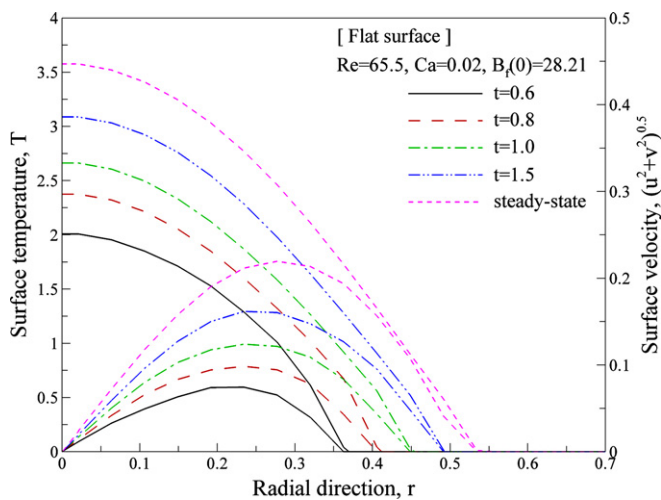
Fig. 13. Transient surface temperature and velocity distributions for a flat surface with $Re = 65.6$, $Ca = 0.02$, and $B_f(0) = 28.21$.
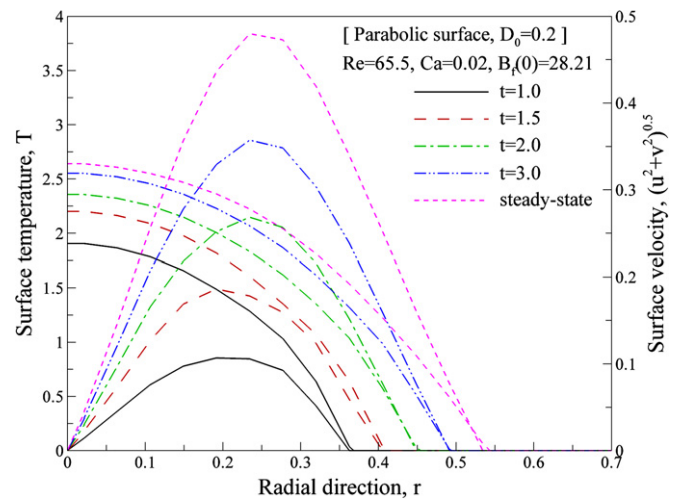
Fig. 15. Transient surface temperature and velocity distributions for a parabolic surface with $Re = 65.6$, $Ca = 0.02$, and $B_f(0) = 28.21$. The values of D_0 and W_0 are 0.2 and 1.0, respectively.

free surface are approximately 61%, 30.1%, and 4.5% of the pool depth lower at the center, respectively, and approximately 0%, 9.4%, and 13.1% of the pool depth lower at the peak, respectively, compared to that of the initial free surface. Also, it can be seen that

the free surface in the molten pool has a concave shape without rim at a higher Re and lower Ca and B_f for the conditions given in

this study. In particular, the reflection point does not change with Re, Ca, and especially B_f, respectively, contrary to those of the flat and parabolic surfaces.

4.3. Transient-state analysis of the laser melting process

Figs. 12 and 13 depict the transient surface deformations and shapes of the melt pool, and surface temperature and velocity profiles with $Re = 65.5$, $Ca = 0.02$, and $B_f(0) = 28.21$ for a flat free surface, respectively. The diameter and depth of the crater, and the thickness and height of the peripheral rim increase monotonically with the increasing width and depth of the molten pool during the laser melting process. The orders of magnitude of surface deformation (crater depth and rim height) are $O(10^{-2})$ and $O(10^{-3})$ at steady-state, respectively, and their values are 1.21×10^{-2} and 4.62×10^{-3}, respectively. Looking at the transient shape of the molten pool and surface temperature and velocity distributions in Figs. 12b and 13, it is evident that the fluid flow at the free surface of the melt pool is radically outward due to the effect of the surface tension gradient driving force, creating a single clockwise rotating flow cell (see Fig. 7c). The melt aspect ratio, defined as the ratio of the width to the depth of the molten pool, decreases from 3.94 to 3.07 over time, because the surface temperature gra-
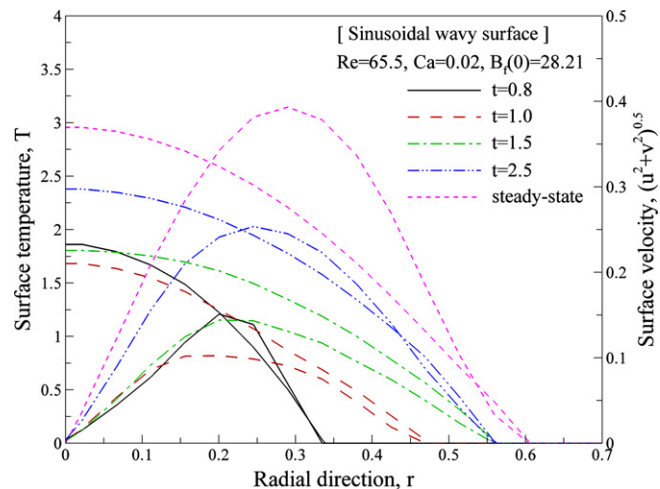

Fig. 17. Transient surface temperature and velocity distributions for a sinusoidal wavy surface with $Re = 65.6$, $Ca = 0.02$, and $B_f(0) = 28.21$. The values of D_0 and W_0 are 0.1 and 0.25, respectively.

dient-induced thermocapillary flow along the free surface occurs actively during the early stage of the melting process.

For a parabolic free surface with $Re = 65.5$, $Ca = 0.02$, and $B_f(0) = 28.21$, the transient surface deformations and shapes of the melt pool, and surface temperature and velocity profiles are illustrated in Figs. 14 and 15, respectively. The width and depth of the molten pool and surface deformations increase gradually with time and at steady-state the orders of magnitude of the crater depth and rim height are the same as $O(10^{-2})$. The values are 3.74×10^{-2} and 1.34×10^{-2}, respectively. The center of the convection cell moves towards the free surface compared to that of the flat surface due to stronger convection as depicted in Fig. 7c and d, and the melt aspect ratio is about 4.34 at steady-state and is approximately 41% larger than that of the flat free surface due to the effect of the curved surface discussed in Section 4.2.1, which causes the pool to be broader and shallower. Fig. 15 shows that the maximum surface temperature decreases by 26% and velocity increases by 119%, compared to those of a flat surface at the steady-state.

Figs. 16 and 17 illustrate the time variation in the free surface deformations and shapes of the melt pool, and surface temperature and velocity profiles with $Re = 65.5$, $Ca = 0.02$, and $B_f(0) = 28.21$ for a sinusoidal wavy surface. In Fig. 16a the height of the free surface at the center decreases until 1 s when the minimum height value is approximately 1.86, and then increases by carrying relatively large amounts of the molten material inward. In this case, the order of magnitude of the surface deformation is $O(10^{-3})$ at steady-state, and its maximum value is 2.77×10^{-2} at $r = 0.29$. As can be seen in Fig. 16b, the melt aspect ratio of about 3.84 at $t = 0.8$ decreases after reaching the maximum value of about 6.49 at $t = 1.5$, and then approaches 4.06 at steady-state due to the inward transfer of the molten material as mentioned previously. In addition, it is noted that at steady-state the maximum surface temperature decreases by approximately 17% and increases by approximately 12%, respectively, and surface velocity increases by approximately 79% and decreases by approximately 18%, respectively, compared to those of flat and concave surfaces.

5. Conclusions

The shape, size, and surface topography of the molten pool in a laser melting process with a curved free surface have been investigated numerically to examine the effects of curved surface shapes and laser power intensity, as well as the thermophysical properties
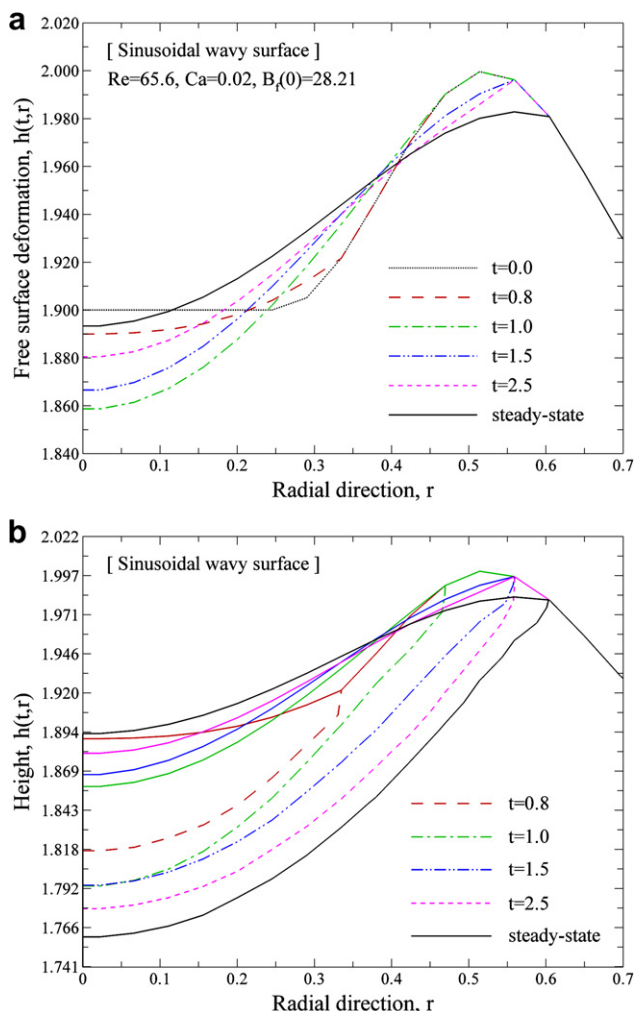

Fig. 16. Transient surface deformation and shape of the molten pool for a sinusoidal wavy surface with $Re = 65.6$, $Ca = 0.02$, and $B_f(0) = 28.21$. The values of D_0 and W_0 are 0.1 and 0.25, respectively.

of material such as Reynolds and Capillary numbers. The results support the following conclusions:

The bump generally has a deep crater at the hot center and a low peripheral rim, because the surface temperature gradient-induced thermocapillary flow drives the molten material towards the cooler region with higher surface tension. For flat and parabolic free surfaces, surface deformations such as crater depth and rim height increase gradually with decreasing Re and increasing Ca, B_f, and the curvature of the free surface. The curvature of the curved free surface has a substantial influence on the shape, size, and surface topography of the molten pool due to enhanced thermocapillary flow compared to that of the flat surface. In particular, it is noted that the curvature of the free surface has little effect on the crater depth and rim height at higher Re and lower B_f with fixed Ca, while its effect is considerably greater at a lower Re and higher B_f indicating stronger convection.

In the case of a sinusoidal wavy surface, it is noted that the crater depth and rim height increase monotonically with increasing Ca at fixed Re and B_f, while they decrease with increasing Re and B_f at fixed Ca by carrying relatively large amounts of the molten material inward compared to the surface tension gradient driving force, causing the recovery of the crater center. Therefore, the slope of the crater decreases significantly. In addition, it is noted that the free surface in the molten pool has a concave shape without rim at a higher Re and lower Ca and B_f for the conditions given in this study. In particular, the reflection point does not change with the variations in Re, Ca, and especially B_f, respectively, contrary to those of the flat and parabolic surfaces.

References

Basu, B., Date, A.W., 1990. Numerical study of steady state and transient laser melting problems – I. Characteristics of flow field and heat transfer. Int. J. Heat Mass Transfer 33 (6), 1149–1163.

Baumgart, P., Krajnovich, D.J., Nguyen, T.A., Tam, A.C., 1995. A new laser texturing technique for high performance magnetic of Ni–P disks. IEEE Trans. Magn. 31 (6), 2946–2951.

Broyden, C.G., 1965. A class of methods for solving nonlinear simultaneous equations. Math. Comput. 19 (92), 577–593.

Chan, C.L., Mazumder, J., Chen, M.M., 1988. Effect of surface tension gradient driven convection in a laser melt pool: three-dimensional perturbation model. J. Appl. Phys. 64 (11), 6166–6174.

Chen, S.C., Cahill, D.G., Grigoropoulos, C.P., 2000. Melting and surface deformation in pulsed laser surface micromodification of Ni–P disks. J. Heat Transfer 122, 107–112.

Fan, H.G., Tsai, H.L., Na, S.J., 2001. Heat transfer and fluid flow in a partially or fully penetrated weld pool in gas tungsten arc welding. Int. J. Heat Mass Transfer 44, 417–428.

Ha, E.J., Kim, W.S., 2005. A study of low-power density laser welding process with evolution of free surface. Int. J. Heat Fluid Flow 26, 613–621.

Ha, E.J., Kim, Y.D., Kim, W.S., 2006. Unified analysis of low-power and high-power density laser welding processes with evolution of free surface, in: Proceedings of the 13th International Heat Transfer Conference, Sydney, Australia.

Han, L., Liou, F.W., 2004. Numerical investigation of the influence of laser beam mode on melt pool. Int. J. Heat Mass Transfer 47, 4385–4402.

Iwamoto, M., Ye, M., Grigoropoulos, C.P., Greif, R., 1998. Numerical analysis of pulsed laser heating for the deformation of metals. Numer. Heat Transfer A – Appl. 34, 791–804.

Kim, W.S., Sim, B.C., 1997. Study of thermal behavior and fluid flow during laser surface heating of alloys. Numer. Heat Transfer A – Appl. 31, 703–723.

Ravindran, K., Srinivasan, J., Marathe, A.G., 1994. Finite element study on the role of convection in laser surface melting. Numer. Heat Transfer A – Appl. 26, 601–618.

Sim, B.C., Kim, W.S., 2005. Melting and dynamic-surface deformation in laser surface heating. Int. J. Heat Mass Transfer 48, 1137–1144.

Sim, B.C., Zebib, A., 2002. Thermocapillary convection with undeformable curved surfaces in open cylinders. Int. J. Heat Mass Transfer 45, 4983–4994.

Sim, B.C., Kim, W.S., Zebib, A., 2004. Axisymmetric thermocapillary convection in open cylindrical annuli with deforming interfaces. Int. J. Heat Mass Transfer 47, 5365–5373.

Srinivasan, J., Basu, B., 1986. A numerical study of thermocapillary flow in a rectangular cavity during laser melting. Int. J. Heat Mass Transfer 29, 563–573.

Swaminathan, C.R., Voller, V.R., 1993. On the enthalpy method. Int. J. Numer. Methods Heat Fluid Flow 3, 233–244.

Willis, D.A., Xu, X., 2000. Transport phenomena and droplet formation during pulsed laser interaction with thin films. J. Heat Transfer 122, 763–770.